LANGMUIR

pubs.acs.org/Langmuir Article

Synthesis of Raspberry-like Nanoparticles via Surface Grafting of Positively Charged Polyelectrolyte Brushes: Colloidal Stability and Surface Properties

Published as part of Langmuir virtual special issue "Highlights in Interface Science and Engineering: Polymer Brushes".

Bashayer Saad Aldakkan, Nikolaos Chalmpes, Genggeng Qi, Mohamed Amen Hammami, Mazen Yousef Kanj, and Emmanuel P. Giannelis*

Cite This: *Langmuir* 2024, 40, 5837–5849 Read Online

ACCESS | Metrics & More | Article Recommendations | Supporting Information

ABSTRACT: A method to synthesize stable, raspberry-like nanoparticles (NPs), using surface grafting of poly(glycidyl methacrylate) (PGMA) brushes on a polystyrene (PS) core with varying grafting densities, is reported. A two-step functionalization reaction of PGMA epoxide groups comprising an amination step first using ethylene diamine and then followed by a quaternization using glycidyltrimethylammonium chloride generates permanently and positively charged polyelectrolyte brushes, which result in both steric and electrostatic stabilization. The dispersion stability of the brush-bearing NPs is dramatically improved compared to that of the pristine PS core in salt solutions at ambient (25 °C) and elevated temperatures (60 °C). Additionally, the grafted polyelectrolyte chains undergo a reversible swelling in the presence of different ionic strength (IS) salts, which modulate the surface properties, including roughness, stiffness, and adhesion. An atomic force microscope under both dry and wet conditions was used to image conformational changes of the polyelectrolyte chains during the swelling and deswelling transitions as well as to probe the nanomechanical properties by analyzing the corresponding force−sample separation curves. The quaternized polyelectrolyte brushes undergo a conformational transition from a collapsed state to a swelled state in the osmotic brush (OB) regime triggered by the osmotic gradient of mobile ions to the interior of the polymer chain. At IS ∼ 1 M, the brushes contract and the globules reform (salted brush state) as evidenced by an increase in the surface roughness and a reduction in the adhesion of the brushes. Beyond IS ∼ 1 M, quartz crystal microbalance with dissipation monitoring measurements show that salt uptake continues to take place predominantly on the exterior surface of the brush since salt adsorption is not accompanied by a size increase as measured by dynamic light scattering. The study adds new insights into our understanding of the behavior of NPs bearing salt-responsive polyelectrolyte brushes with adaptive swelling thresholds that can ultimately modulate surface properties.

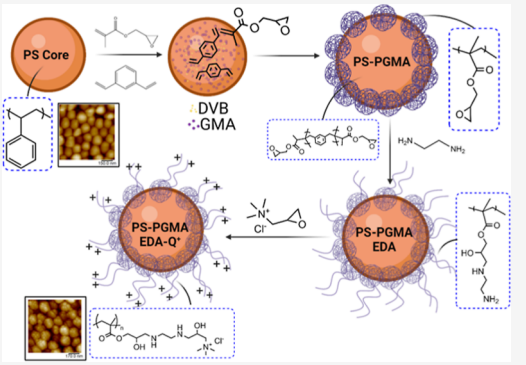

INTRODUCTION

Stability of colloidal dispersions has been researched widely for a multitude of applications, including drug therapy,[1] bioimaging,[2] oil recovery,[3] and geothermal energy production.[4] A common strategy to counterbalance the van der Waals attraction leading to particle aggregation is to introduce electrostatic or steric motifs that shield and, thus, prevent the particles from approaching close together.[5,6] Electrostatic stabilization results because of an electrical double layer comprising an immobile Stern plane (counterions with a charge opposite to the particle surface charge) and a diffuse layer (a layer of mobile ions), which can be easily disrupted in various electrolytes (i.e., in the presence of charge-screening ions).[7] Hence, electrostatic stabilization strategies that work well in salt-free environments become less effective in the presence of even low ionic strength (IS) electrolytes. On the other hand, steric stabilization can be realized by tethering polymer chains onto the particle surface. In that case, Brownian collisions between particles result in both entropic and enthalpic repulsions caused by the interpenetration and/or compression of approaching polymer chains.[8] However, to achieve sufficient steric stabilization, the adsorbed ligands/polymer layers must be well solvated in the solvent with a minimum required thickness dictated by the particle size and

Received: December 1, 2023
Revised: February 28, 2024
Accepted: February 29, 2024
Published: March 8, 2024

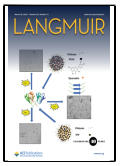

https://doi.org/10.1021/acs.langmuir.3c03713
Langmuir 2024, 40, 5837−5849

Scheme 1. (1) Amination of Epoxide the Ring of PGMA Using EDA; (2) (a) Quaternization Reaction of PGMA-EDA with GTMAC to Synthesize PGMA Brush; (b) Side Reaction with Neighboring PGMA Chains to Yield Interchain Bridges

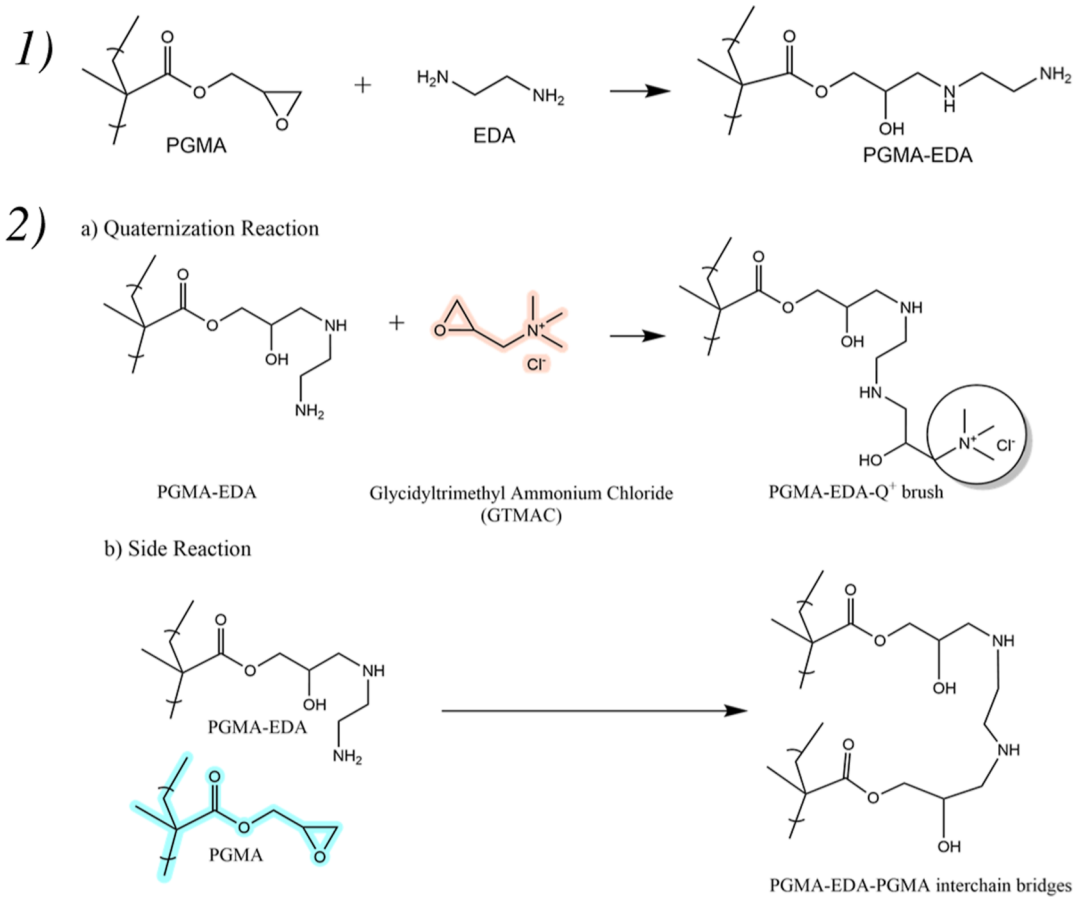

the magnitude of the Hamaker constant.[9] Ligand and polymer solvation is significantly reduced in high IS concentrated brines and high temperatures.[10] Another strategy, which combines the two approaches described above, is accomplished by using charged, extended polymer chains (polyelectrolyte brushes). This last approach provides colloidal stabilization by combining both electrostatic and steric repulsive forces.

Polymer brushes tethered onto various surfaces and/or interfaces with specific functionalities have resulted in advances not only in colloidal stabilization[11] but also in drug delivery,[12] surface coatings,[13] implantable devices,[14] soft robotics,[15] surfactancy,[16,17] and sensing.[18] By adopting multiple conformational states, the polymer brushes can be tuned to respond to specific changes, including the type of solvents,[19,20] ions,[21,22] pH,[23] and temperature.[24,25] These different stimuli can trigger rapid transitions and can control the structure and properties of the polymer brushes, including entanglements, hydration, swelling, wetting, adhesion, and friction.[26]

Polymer-grafted nanoparticles (NPs) can be tuned to exhibit desirable thermal and mechanical properties by tailoring the chemistry, grafting density, and flexibility of the attached chains.[27] Choi et al.[28] evaluated the mechanical properties of polystyrene(PS)-poly(methyl methacrylate) brushes grafted on silica particles and the transition from "hard-sphere-like" to "polymer-like" mechanical behavior depending on the degree of polymerization. Yang et al.[16] developed responsive, single-chain/colloid Janus particles based on poly(2-(2-methoxyethoxy)ethyl methacrylate chains on Fe_3O_4 NPs. These chains can segregate at surfaces/interfaces like surfactants and can undergo amphiphilic/hydrophobic transitions with heating or using near-infrared irradiation. In another study, Lotierzo et al. reported the synthesis of anisotropic, Janus particles by cross-linking *n*-butyl methacrylate cores with poly(methyl methacrylate-methacrylic acid)-*block*-poly(*n*-butyl methacrylate) copolymer micelles and used them as colloidal stabilizers for the emulsion polymerization of styrene.[29]

Incorporating reactive functional sites within the polymer brush architecture is of particular importance to modulate properties and control performance. Examples include monomers containing vinyl groups, epoxides, sulfates, and amines. Glycidyl methacrylate (GMA) is such an example of a functional monomer with reactive electrophilic carbons in a strained 3-membered ring that can undergo ring-opening reactions by various nucleophiles, including amines,[30] alcohols,[31] azides,[32] carboxylic acids,[33] thiols,[34] and water.[35] Puretskiy and Ionov[36] synthesized poly(glycidyl methacrylate) (PGMA) grafted onto silica to yield "raspberry-like" particles with a good stability and mechanical performance as well as a coupling agent for ultrahydrophobic coatings.

In this study, we leverage the chemistry of PGMA to graft polyelectrolyte brushes onto NP cores. Specifically, we report the synthesis of raspberry-like NPs composed of latex PS cores decorated with cationically charged PGMA brushes. The synthesis is based on a two-step amination process of pendant PGMA epoxide segments attached to PS cores (Scheme 1). The first step is based on ethylene diamine (EDA)-assisted ring-opening reaction of the GMA epoxide groups followed by

https://doi.org/10.1021/acs.langmuir.3c03713
Langmuir 2024, 40, 5837−5849

the introduction of permanently charged, quaternary ammonium groups using glycidyltrimethylammonium chloride (GTMAC). The resulting pendant cationic moieties control flocculation of the resulting colloidal suspensions, leading to highly stable systems even at high-temperature/high-salinity environments. The colloidal properties of the NPs and their salt adsorption/swelling behavior in various electrolytes were probed by dynamic light scattering (DLS), accelerated dispersion stability, and quartz crystal microbalance (QCM) measurements. The raspberry-like motifs of the brushes on the NPs undergo morphological transitions in the presence of various ion electrolytes, and the corresponding changes in surface and nanomechanical properties (including roughness, stiffness, and adhesion) were characterized by an atomic force microscope equipped with a fluid cell. The colloidally stable NP suspensions developed in this study can be potentially deployed in a number of practical applications including those in aggressive and demanding environments such as in oilfield applications, where the NPs can be suspended and injected with the seawater (SW). The NPs can serve as tracers or delivery systems to alter interfacial properties, and they can be recovered ultimately upon production.[37,38]

MATERIALS AND METHODS

Materials. Styrene (≥99%), Nile red (≥97%), [2-(acryloyloxy)-ethyl]trimethylammonium chloride solution (80 wt % in H_2O) (AOETMAC), divinylbenzene (DVB) (para and meta isomers) (80%), EDA (≥99%), GTMAC (≥90%) and 2,2′-azobis(2-methylpropionamidine) dihydrochloride (granular, 97%) (V50), sodium chloride (NaCl) (99%), calcium chloride dihydrate ($CaCl_2{\cdot}2H_2O$) (98%), magnesium chloride hexahydrate ($MgCl_2{\cdot}6H_2O$) (99%), sodium sulfate (Na_2SO_4) (99%), and sodium bicarbonate ($NaHCO_3$) (99.7%) were all purchased from Sigma-Aldrich. GMA (>95%) was purchased from TCI chemicals, and *N*-hexadecane (99%) was purchased from Alfa Aesar. Cetyltrimethylammonium bromide (CTAB) (≥99%) was purchased from Amresco. A regenerated cellulose dialysis tubing with 3.5k molecular-weight cutoff (MWCO) was purchased from Thermo Fisher Scientific. All chemicals were used as received without further purification. Stock solutions of SW (*IS*∼ 1.14 M) and high-salinity water (HSW) (*IS*∼ 2.5 M) (amounts listed in Table S1) were prepared and used to test the colloidal stability of the various NP systems.

Synthesis of Fluorescent Poly(styrene), NP Cores. PS NP cores were synthesized using free-radical, miniemulsion polymerization with deionized (DI) water as the dispersion medium. For the aqueous phase, 1.4 g of CTAB, 0.74 g of AOETMAC comonomer, and 0.566 g of V50 initiator were mixed in 400 mL of DI water. The oil phase, comprising 3 mg of Nile red, 62 g of styrene, and 2 g of hexadecane, was added to the aqueous phase, and the mixture was sonicated with an ultrasonic probe (Branson SFX150) at 50% amplitude of the sonicator power for 20 min to produce a seed, oil-in-water emulsion stabilized by the cationic surfactant and comonomer. Hexadecane is used to stabilize the emulsion seeds by creating an osmotic pressure that prevents coalescence of oil droplets into a macroemulsion by Ostwald ripening.[39,40] The mixture was heated at 70 °C for 24 h using continuous stirring under a N_2 flow to initiate polymerization.

Grafting of PGMA Brushes to Synthesize PS-PGMA NPs (S21, S31, and S41). PGMA was grafted to the surface of the PS cores using different molar ratios of PS to PGMA (i.e., 2:1, 3:1, and 4:1 corresponding to S21, S31, and S41, respectively) with DVB as a cross-linker. In a typical grafting experiment, a stock mixture of GMA/DVB containing 2.38/0.014 g, 3.1/0.019 g, or 4.7/0.028 g (for S41, S31, and S21, respectively) was prepared. 1 mL of this mixture was added to 50 g of the PS cores stock, and the solution was stirred continuously at room temperature for 24 h to allow the monomer mixture to diffuse into the particle cores. 0.045, 0.06, and 0.09 g of V50 initiator (for S41, S31, and S21, respectively) were dissolved in 5 mL DI water and added into the stirred solution, after which the remaining GMA/DVB mixture was added in a dropwise fashion (Fisherbrand Single Syringe Pump) at 2 mL/h. The mixture was stirred at 500 rpm and allowed to react at 60 °C for 24 h.

Amination of PS-PGMA with EDA. 11.2 g of the resulting PS-PGMA suspension was taken out of the stock solution to which 0.059, 0.777, and 1.134 g of EDA in 4 mL of DI water were added for S41, S31, and S21, respectively, and the mixture was stirred at 350 rpm while kept at 50 °C for 48 h. EDA was added in excess (3× molar concentration of GMA) to drive the reaction with the epoxide groups to completion and form PGMA-EDA brushes on the surface of PS NPs [PS-PGMA-EDA, Scheme 1(1)]. The resulting solution was then dialyzed using 3.5k MWCO tubing to remove any residual EDA.

Quaternization Reaction to Synthesize S21+, S31+, and S41+. After dialysis, the suspension of PGMA-EDA functionalized PS NPs was sonicated for 30 min after which 3 mL of GTMAC in 3 mL of DI water was added gradually and allowed to stir at 50 °C. In this last step, the quaternary ammonium groups of GTMAC react with the pendant amine groups of PGMA-EDA through a second epoxide ring opening as shown in Scheme 1(2a). It is worth mentioning that the pendant amine groups can also react with a neighboring PGMA epoxide ring [Scheme 1(2b)]. After the reaction, the particle suspensions were dialyzed using 3.5k MWCO tubing before further characterization.

NP Characterization. The size and zeta potential (ZP) of the NPs were measured using a DLS Zetasizer Nano 90 (Malvern Panalytical). Scanning electron microscopy (SEM) and transmission electron microscopy (TEM) images were obtained by using a Zeiss Gemini 500 SEM and an FEI Tecnai 12 BioTwin TEM, respectively. Thermogravimetric analysis (TGA) of the PS core and PGMA-grafted NPs used to estimate the PGMA content at different grafting ratios was performed on a TA Instruments 5500 Thermogravimetric Analyzer under a N_2 flow at a heating rate of 5 °C/min up to 700 °C. Fourier-transform infrared (FTIR) spectra were collected on a Thermo Scientific FTIR spectrometer. AFM measurements were conducted using a Bruker MultiMode 8-HR AFM.

LUMiSizer Dispersion Stability Analysis. The colloidal stability of the NPs was tested using 0.1 and 0.5 wt % dispersions of the NPs in single and mixed salt electrolytes. Aliquots of 0.45 μL of the different dispersions were placed in the LUMiSizer cell and filled below the meniscus height, which is estimated by the software to be ∼105 mm. Samples were centrifuged at 1000 rpm (117× gravitational acceleration) for 50 min, and the transmission across the sample was measured as a function of time in 10 s increments using light illumination (870 nm). From these measurements, the separation indices (SIs) at 25 and 60 °C were calculated as follows. Initially, at time zero, t_0, the transmission through the sample is low because of the presence of particles in the suspension. If the suspension is colloidally stable, then no change in transmission is recorded with time. For samples, where particle sedimentation takes place, the transmission in the middle of the sample increases with time as the particles sediment at the bottom of the cell, where the transmission decreases.

QCM with Dissipation Monitoring. Salt sorption was quantified using a Biolin Scientific Q-Sense instrument by measuring the frequency shift (ΔF) and dissipation (ΔD) of samples deposited on Au-coated QSX 301 quartz crystal sensors (Nanoscience Instruments). The sensors were first UV/ozone treated for 10 min and submerged for 5 min in a mixture of 5:1:1 [DI water, ammonia (25%), and hydrogen peroxide (30%)] heated to 70 °C followed by a rinse with DI water and drying with N_2. The sensors were then treated with UV/ozone for 10 min before drop casting 100 μL of 0.05 wt % of the sample suspension (filtered through a 0.45 μm syringe filter to establish a uniform layer and remove any aggregates). At the beginning of each measurement, DI water was injected first to establish a stable baseline followed by continuous injection of different electrolyte solutions until equilibration for at least 15 min and before a final DI water wash. Shifts in ΔF and ΔD were collected using the 3rd to 13th overtones. Since the films behave

https://doi.org/10.1021/acs.langmuir.3c03713
Langmuir 2024, 40, 5837−5849

viscoelastically, the amount of salt adsorption in response to the variation in IS of the electrolyte was calculated using the Kelvin−Voigt model. Briefly, a shear stress applied to the film by the oscillating crystal results in both elastic (spring) and viscous (dashpot) contributions to the stress/strain relation, which can be represented by eq 1[41]

$$\sigma_{xy} = \mu \frac{\partial u_x(y,t)}{\partial y} + \eta \frac{\partial v_x(y,t)}{\partial y} \quad (1)$$

where μ is the shear modulus of the film, η is the shear viscosity of the film, and u_x and v_x represent the displacement and velocity in the x-direction, respectively. Using the Taylor expansion, the film viscoelastic properties [including viscosity, density, shear modulus, and thickness (mass)] can be obtained by fitting the measured ΔF and ΔD to eqs 3 and 4 at different overtones[42,43]

$$|\Delta F| \cong \frac{1}{2\pi\rho_q t_q} t_f \rho_f \omega \left(1 + \frac{2t_f^2 \chi}{3\delta^2(1+\chi^2)}\right) \quad (2)$$

$$\Delta D \cong \frac{2t^3 \rho_f f}{3\pi f_0 \rho_q t_q} \frac{1}{\delta^2(1+\chi^2)} \quad (3)$$

$$\chi = \frac{1}{\tan\delta} = \frac{u_f}{2\pi f \eta_f} \quad (4)$$

$$\delta = \sqrt{\frac{2\eta_f}{\rho_f f}} \quad (5)$$

In the above, ρ_q and t_q are the density and thickness of the quartz crystal, respectively; ρ_f and t_f are the density and thickness of the film; χ is the inverse of the mechanical loss tangent; f and f_0 are the measured and resonance frequencies, respectively; and δ is the viscous penetration depth. The Kelvin−Voigt viscoelastic parameters were fitted to the collected frequency and dissipation data at various overtones using Q-tools software (Biolin Scientific).

AFM Measurements. AFM was performed using the PeakForce Tapping mode with a ScanAsyst-fluid nitride coated silicon tip (spring constant of 0.7 N/m). The AFM tip was calibrated against a sapphire standard to obtain its actual deflection sensitivity as well as the spring constant and its radius that were used in the nanomechanical property calculations. The deflection sensitivity was 21.54 nm/V using a single ramp run (approach-retraction) with a spring constant of 0.516 N/m using thermal tuning. These calibration parameters were entered in NanoScope 6 software before each subsequent measurement. For the sample preparation, a 0.05 wt % suspension of the particles was filtered through a 0.45 μm syringe filter, and a few drops were deposited on a Si-wafer (p-type, purchased from Pure Wafer). Prior to drop casting, the Si-wafers were submerged in an ethanol solution and placed in an ultrasonic bath for 15 min (160 W) followed by washing with DI water. For measurements in fluid environments, a liquid cell was used, and a droplet of the corresponding liquid was added on the sample surface as well as on the tip and allowed to equilibrate for 30 min. Force−separation curves were collected and analyzed. The stiffness of the samples was calculated from the linear part of the retrace curve, while the adhesion was obtained from the minima of the same curve.[44]

RESULTS AND DISCUSSION

The polyelectrolyte-grafted, raspberry-like NPs with different grafting densities (S21+, S31+, and S41+) are synthesized according to the following four steps: (1) synthesis of the PS cores by emulsion polymerization of styrene; fluorescent dyes to add imaging capabilities can be incorporated in this step, (2) swelling of the PS cores using a mixture of GMA/DVB to incorporate the brush precursor, followed by a polymerization reaction to form PGMA. Since the resulting PGMA chains are immiscible with PS, they phase-separate and form raspberry-like patches on the surface of the PS cores, (3) reaction of the patches with EDA via ring opening of the epoxide groups of PGMA, and (4) reaction of the amine groups with the glycidyl trimethylammonium chloride (GTMAC) that leads to the permanently charged, polyelectrolyte brushes grafted to the PS particle surface.

The size of the PS cores obtained from DLS measurements after the emulsion polymerization is ∼91 nm with a ζ-potential of +37 mV. The positive charge of the cores before grafting of the polyelectrolyte brushes is due to the presence of CTAB and the quaternary ammonium comonomer (AOETMAC), which are added to facilitate the emulsion polymerization reaction. For the next step, three different ratios of PS to GMA were used to synthesize particles with different brush densities: 2:1, 3:1, and 4:1 referred to as S21, S31, and S41, respectively. To generate the positively charged polyelectrolyte brushes, first EDA and then GTMAC were added in the two subsequent steps (Scheme 1). We note that in addition to the desired reaction, the reactive epoxide groups can also undergo an amine-induced ring opening by neighboring PGMA chains to form bridges between the chains [Scheme 1(2b)].

The NP systems produced after different steps were characterized by TEM, SEM, and AFM (Figure 1). The microscopy images show relatively monodispersed particles for both the core and PGMA functionalized particles. However, the latter exhibit a rough surface with multiple lobes (in contrast to the core particles, which possess a smooth surface; Figure 1). FTIR spectroscopy (Figure S1) confirmed the grafting of the PGMA brushes to the core NPs. The peak at 1723 cm^{-1} is attributed to the presence of carbonyl groups due to GMA. At the same time, the asymmetric stretch of the epoxide ring at 942 cm^{-1} disappears because of the ring-opening reaction. In addition, the broad peak centered around 3395 cm^{-1} is assigned to hydroxyl and possibly amine groups (both the N−H and O−H stretching modes appear in this wavelength range). TGA (Figure S2) reveals two clear thermal decomposition regimes corresponding to the degradation of the quaternized PGMA brushes (between 250 and 300 °C) and the degradation of the PS cores (between 350 and 400 °C). The amount of the PGMA brushes is calculated at 11.5, 14.7, and 23 wt % for S41+, S31+, and S21+, respectively.

The size distribution and ZP for the core- and brush-grafted NPs are shown in Figure S3 and summarized in Table 1. In all systems, positively charged particles with an estimated brush thickness of 12−20 nm in DI water (i.e., salt-free environment) are obtained. As stated earlier, the PS cores do bear a positive charge due to the presence of AOETMAC added as part of the emulsion polymerization reaction. Despite the presence of the positive charge, the PS cores aggregate quickly when suspended in SW. In contrast, the polyelectrolyte-grafted NPs increase in size but are stable in SW. As stated below in detail, the brush charge and configuration depend on the surrounding medium, particularly in the presence of charge-screening ions. The presence of amine groups along the brush backbone suggests that these NPs should be responsive to changes in the pH (Scheme 2). The ZP measurements of the particles at different pH show that the NPs stay positively charged even above the pK_a values of isolated EDA (∼10.21 and 7.16). For example, the ZP at pH 12, where the two amine groups are deprotonated, is ∼+23 mV due to the presence of the terminal quaternary ammonium groups.

Characterization of Colloidal Stability via Accelerated Testing. We next probe the stability of the particles

https://doi.org/10.1021/acs.langmuir.3c03713
Langmuir 2024, 40, 5837−5849

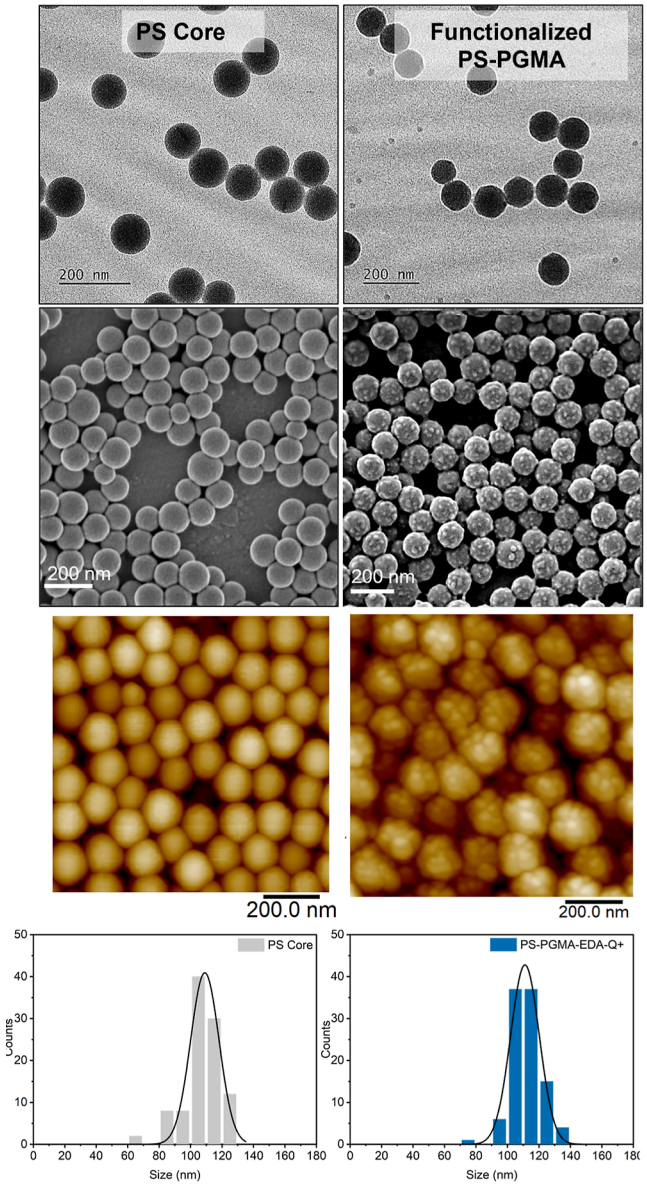

Figure 1. TEM, SEM, and AFM (in dry conditions) images for PS core NPs and S31+ [PS-PGMA-EDA-Q+ (3:1) ratio] with the corresponding size distribution obtained from TEM images.

suspended in SW using accelerated sedimentation tests. The transmission profiles and corresponding SI were measured for both the PS core and the polyelectrolyte-grafted particles in SW at two temperatures (25 and 60 °C) before and after amination (Figure S4). Note that as the particle suspension in the cell is subjected to centrifugation, if stable, its transmission remains unchanged with time over its entire length (and the SI is ∼0). In contrast, when the suspension is not stable, the transmission increases with time at the top of the cell and decreases at the bottom as the particles begin to sediment (the SI is 1 for completely sedimented suspensions). The transmission profile over time for a 0.5 wt % suspension of the PS core changes with time, suggesting a low colloidal stability. Similar behavior is observed for suspensions of PS-PGMA NPs prior to amination and quaternization. Note that the stability remains low for these systems, even at lower particle concentrations. We hypothesize that the PGMA chains on the surface prior to the amination and quaternization do not provide sufficient steric stabilization probably due to their relatively short length. The effect is exaggerated because of the unfavorable mixing with water, which acts as a poor solvent for PGMA. In contrast, to the previous systems, NP suspensions of S41+, S31+, and S21+ show an excellent colloidal stability. The SI decreases from 0.75 for the PS core to ≤0.004 and ≤0.037 at 25 and 60 °C, respectively. Since the functionalization of the brush consists of two steps (amination and quaternization), an accelerated sedimentation test was conducted for the particles decorated with brushes after reaction with EDA but prior to quaternization (PS-PGMA-EDA). The transmission profiles (Figure S5) are consistent with an unstable suspension after only the amination step, suggesting that the quaternization step is essential for colloidal stability.

Swelling Behavior in Response to Varying ISs. Polyelectrolyte chains are prone to swelling when suspended in either a good solvent due to the favorable solvent−polymer interactions that maximize the polymer−solvent contact area or salt solutions as the osmotic pressure gradient can trigger diffusion and absorption of counterions in the interior of the brush.[45] This swelling is counterbalanced by an elastic retractive force due to the reduced entropy by the segmental chain stretching that decreases the entropically accessible configurations.[46,47] Capturing the swelling thresholds for the grated polymer chains is desirable to modulate surface properties, including roughness, stiffness, and adhesion. Detailed size measurements in the presence of various electrolytes (NaCl, Na_2SO_4, and $MgCl_2$) were conducted using suspensions of S31+ as a model system. All S31+ suspensions appear stable (low SI values) under these conditions (Figure S6). As shown in Figure 2, the particle size first increases with increasing IS due to the swelling, but

Table 1. Size and ZP Recorded for PS Core, PS-PGMA, and PS-PGMA-EDA-Q+ NPs in DI Water and SW at Different Molar Ratios Using DLS[a]

sample (PS:PGMA ratio)	PS core		PS-PGMA		PS-PGMA-EDA-Q+	
	size (nm)	ZP (mV)	size (nm)	ZP (mV)	size (nm)	ZP (mV)
S41 (4:1)	91 ± 8[b]	+37 ± 1.5[b]	94 ± 4[b]	+28 ± 0.1[b]	114 ± 10[b]	+38 ± 0.4[b]
	4450 ± 625[c]				139 ± 5[c]	
S31 (3:1)			107 ± 13[b]	+32 ± 1.3[b]	125 ± 6[b]	+39 ± 1.1[b]
					147 ± 1.2[c]	
S21 (2:1)			116 ± 2[b]	+31 ± 0.2[b]	131 ± 9[b]	+39 ± 1.9[b]
					151 ± 3[c]	

[a]See Supporting Information (Figure S3 for distribution plots). [b]Measurement of NP suspension in DI water. [c]Measurement of NP suspension in SW.

https://doi.org/10.1021/acs.langmuir.3c03713
Langmuir 2024, 40, 5837−5849

Scheme 2. Protonation States of Isolated EDA at Equilibrium pK_a Values of ~10.21 and 7.16

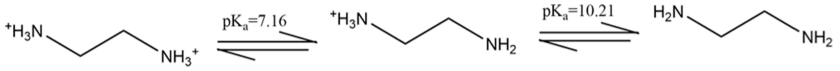

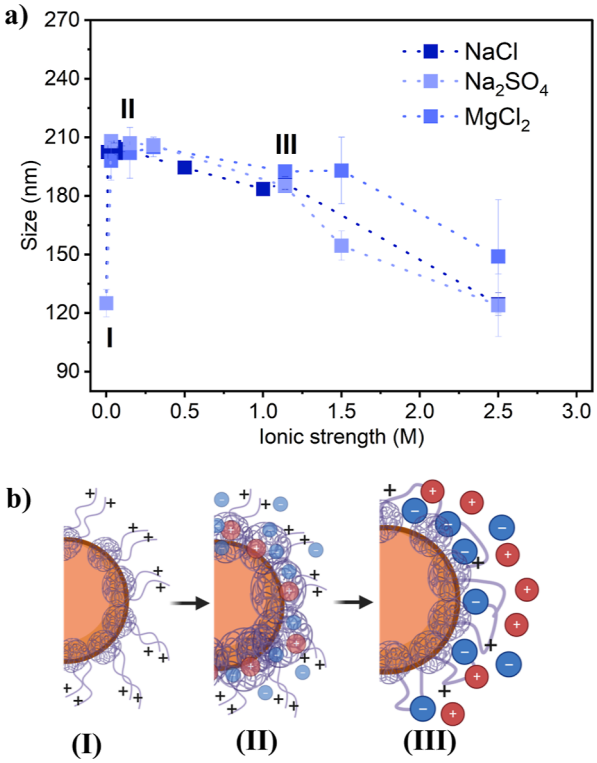

Figure 2. (a) Brush-grafted NP size (S31+) obtained by light scattering as a function of IS in individual salts (NaCl, Na_2SO_4, and $MgCl_2$) and (b) schematic representation of the configuration of the polycationic brushes with increasing IS: (I) collapsed/globular brush, (II) OB, and (III) SB.

the swelling is nonmonotonic consistent with the behavior observed for most polyelectrolytes in salt solutions.[46,48] The brush configuration can adopt three states (Figure 2b): (i) collapsed (or pinned micelles) brush (CB), (ii) swollen, osmotic brush (OB) driven by the osmotic gradient and consequent salt diffusion in the interior of the brush, and (iii) partially retracted state, also called the salted brush (SB) regime, when ions are expelled from the brush interior due to saturation/screening and multivalent counterion condensation of two single-charged monomer units. In the latter state, ion adsorption can still take place predominantly on the outer surface of the brush.[49,50] In the CB state, as demonstrated by Zhulina and co-workers,[51] the equilibrium configuration is driven by a balance of three contributing forces: (i) surface free energy of the brush with the surrounding solvent (ΔF_{surf}), (ii) free energy associated with the elastic stretching of the anchoring segments/legs (ΔF_{leg}), and (iii) electrostatic free energy of the charged monomer units (ΔF_{elec}).

When there is no salt present, the polyelectrolyte chains adopt a collapsed conformation (thickness of ~17 nm). As the electrolyte IS increases from 0.01 to 1 M, the polyelectrolyte chains undergo gradual swelling transitioning from the CB state to the OB state. The transition from the collapsed state to the swollen state results in a maximum increase of ~37 nm in brush thickness for NaCl, Na_2SO_4, and $MgCl_2$ at concentrations between 0.01 and 0.3 M. After that, there is no more swelling (no increase in size). Finally, the size decreases as the brushes begin to collapse at higher salt concentrations (IS = 1−2.5 M).

In the presence of salts, polyelectrolyte brushes can experience different ion concentrations inside and outside the chains, which results in an osmotic pressure difference. As the IS of the medium outside the brushes increases, more and more ions diffuse into the interior to reduce the ion imbalance.[52,53] The extent of swelling depends on many factors including the cross-linking density, the grafting ratio, the chain length, and the hydrating power of the diffusing ions. Since the hydrated SO_4^{2-} is larger (3.79 Å) compared to Cl^{-1} (3.32 Å), a larger increase in the NP size is observed for that system.[54−56] As the concentration of ions in the bulk electrolyte approaches the concentration of ions within the brush, chain contraction takes place due to the charge screening/counterion saturation that induce local charge inversion, which reduces the electrostatic repulsion between like-charged units.[57] Furthermore, in the case of multivalent counterions (e.g., SO_4^{2-}), electrostatic interactions can bridge two single-charge monomer units.[58] For this reason, the chain contraction and particle size decrease are more pronounced for sodium sulfate compared to those of the other salts up to 2.5 M. The DLS trends are consistent with AFM measurements (Figure S7). The somewhat smaller size obtained by AFM compared to the size obtained from light scattering (~10% difference) is probably due to that DLS measurements are performed in very dilute suspensions, while the AFM measurements involve highly concentrated samples deposited on a substrate, where swelling might be hindered by crowding by neighboring particles.

QCM with dissipation monitoring (QCM-D) measurements were used to quantify the salt adsorption in electrolytes of various ISs and correlate with the swelling experiments described above. Changes in frequency (ΔF) and dissipation (ΔD) were recorded for NaCl (Figure S8), Na_2SO_4, $MgCl_2$, and SW. The transition from the CB conformation to the swollen state is accompanied by viscous effects, as the swollen flexible chains lead to higher energy dissipation. The proposed flexible, extended brush configuration in the OB regime and in the partially retracted SB regime shows increased dissipation, as flexible chains are reported to couple poorly with the resonant oscillations of the sensor.[59] The salt adsorption is reversible, as subsequent washes with DI water cause a reverse pressure gradient, and salt ions begin to diffuse out of the brush interior into the bulk water, as evidenced by the return to the initial values of frequency and dissipation (Figure S8 a). This reversible association is expected as counterions that are in close proximity to the chains are electrostatically associated rather than immobilized at specific sites.[60] It is worth noting that a slight secondary adsorption is observed during the washing process, which could be due to the hydration of the patches as incorporated salt ions are switched with the solvent.

Starting with the simple monovalent salt NaCl, Figure 3 shows the reduction in frequency when the QCM was immersed in various NaCl solutions. The areal mass was obtained by fitting the data to the Kelvin−Voigt model. The gradual increase in size in the OB state (stage II) is

https://doi.org/10.1021/acs.langmuir.3c03713
Langmuir 2024, 40, 5837−5849

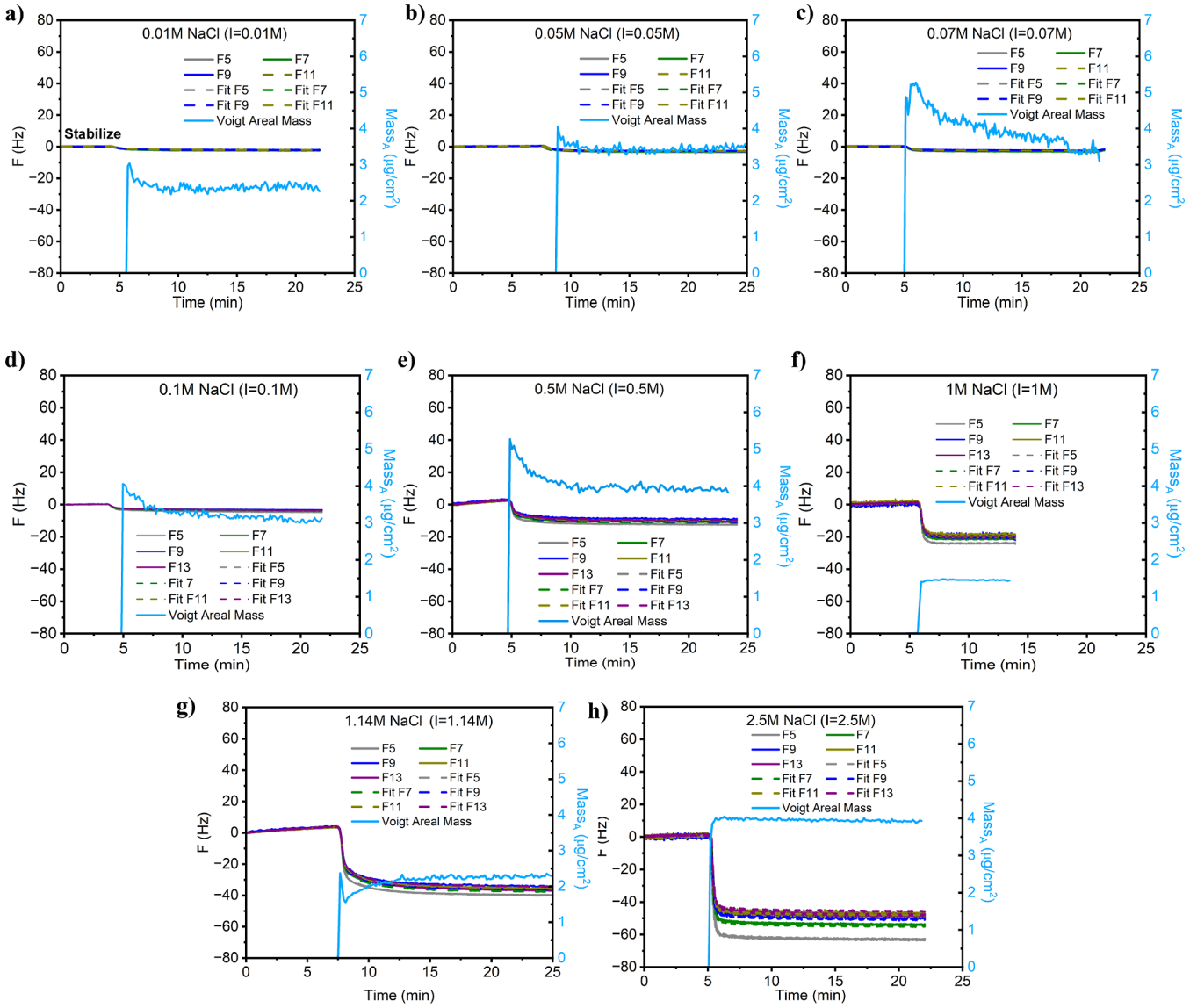

Figure 3. Experimentally measured and modeled frequency profiles from QCM-D with calculated areal mass as a function of time at different NaCl ISs after stabilization in DI water: (a) 0.01, (b) 0.05, (c) 0.07, (d) 0.1, (e) 0.5, (f) 1, (g) 1.14, and (h) 2.5 M.

accompanied by a gradual increase in salt absorption (the areal mass increases to ~3.9 μg/cm^2 at $I \sim 0.5$ M). As the brushes on the NPs transition to SB or stage III, a decrease in salt adsorption is observed due to the ion expulsion from the interior of the brushes (the adsorbed mass decreases from 3.9 to 1.4 μg/cm^2). After that, the salt adsorption increased back to 3.9 μg/cm^2. In this stage, most of the ions are adsorbed predominantly on the exterior of the brushes caused by counterion saturation. In the case of SW (Figure S9a), the amount of salt adsorbed was ~2.3 μg/cm^2, which is equal to the amount adsorbed in the presence of NaCl at an equivalent IS of ~1.14 M. Figure 4 summarizes the frequency and dissipation profiles and the calculated areal masses for different salts. For Na_2SO_4 (Figures 4b and S9b), the maximum salt uptake during the swelled state is ~8 μg/cm^2 at $I \sim 0.15$ M. The areal mass stays relatively constant (3.2−3.7 μg/cm^2) for solutions with ISs of 1.14−1.5 M, where the transition from OB to SB takes place. Further increase in the adsorbed salt reaching up to 4.9 μg/cm^2 at 2.5 M salt is attributed to adsorption on the exterior of the brushes as they enter the SB state or stage III. Similar behavior is observed for $MgCl_2$ with a maximum salt uptake of 8.8 μg/cm^2 in the OB regime, followed by a reduction in the salt adsorption during the transition to the SB regime. At a low salt concentration on the other hand, and as the brushes become swollen, the amount of salt adsorbed differs depending on the character of the ions. Higher salt adsorption is reported for Na_2SO_4 and $MgCl_2$ in comparison to NaCl in the OB state since monovalent salts, such as NaCl, have a strong tendency to screen long-range electrostatic interactions that drive more ions from the bulk solution to the NP surface, compared to screening short-range lateral correlation between the charged patches. Hence, this screening diminishes the binding with the NPs resulting in lower amounts of NaCl absorbed.[61] During the SB regime, external ion association is the same for all salt solutions, which is lower compared with the amount of salt incorporated and diffused within the network in the OB regime.

Surface topographical and nanomechanical properties before and after grafting of the polyelectrolyte brushes as well as in contact with different fluids were probed using AFM. In the

https://doi.org/10.1021/acs.langmuir.3c03713
Langmuir 2024, 40, 5837−5849

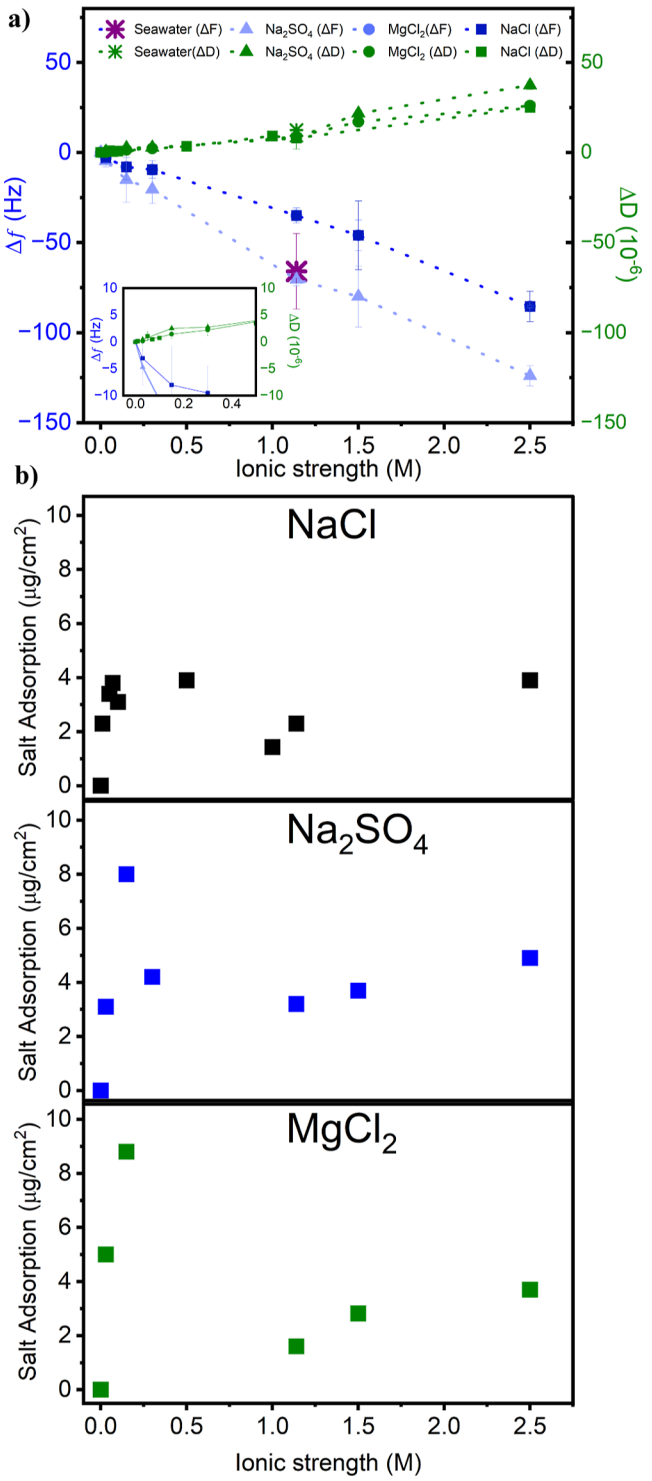

Figure 4. (a) Changes in frequency, ΔF and dissipation, ΔD of S31+ after salt adsorption; (b) calculated areal mass adsorbed during different regimes (the OB configuration is observed between 0.01 and 1 M, and the SB configuration is observed between 1 and 2.5 M) for NaCl, Na_2SO_4, and $MgCl_2$ using the Kelvi−Voigt model. Dashed lines are added as a guide to the eye.

experiment as the tip approaches and then retracts from the sample, the force at different tip−sample separation is measured.[62] Stiffness can be calculated from the linear part of the retrace part of the force−separation graph, while the minimum in the retrace part of the graph corresponds to the adhesion between the AFM tip and the sample. Figures 5 and 6 summarize the nanomechanical response to an applied force as

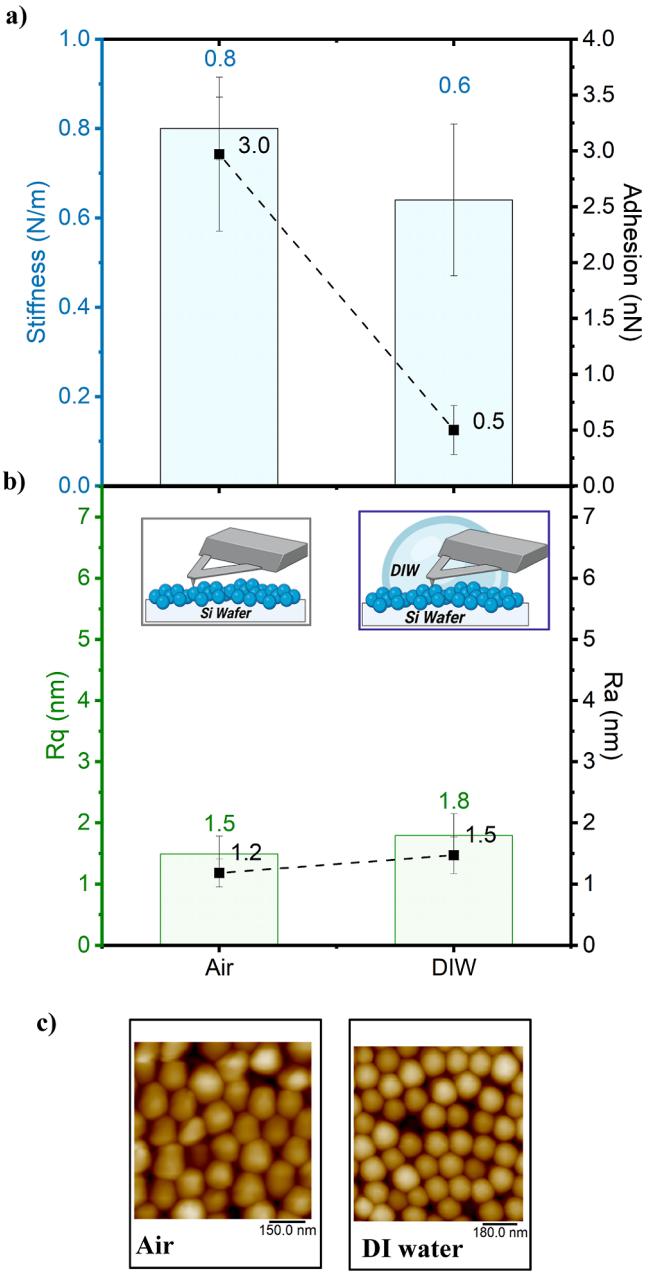

Figure 5. (a) Quantitative nanomechanical (QNM) properties (stiffness and adhesion) for the PS core; (b) roughness (root mean square, R_q, and average values, R_a) in air and in DI water using a AFM-peak force tapping mode; and (c) corresponding images in dry conditions (left) and in DI water (right).

well as the surface roughness of the core and polyelectrolyte-grafted particles, respectively. The PS cores exhibit similar stiffness in both dry and wet conditions; on the other hand, adhesion in DI water is reduced compared to that under dry conditions. The higher adhesion is expected as the presence of humidity results in attractive capillary forces between the tip and the dry sample, which is independent of the tip−sample intrinsic interactions.[63] The smooth surface of the pristine PS core shown previously in the SEM images (Figure 1) results in low roughness values (1.5 and 1.8 nm when dry and in DI

https://doi.org/10.1021/acs.langmuir.3c03713
Langmuir 2024, 40, 5837−5849

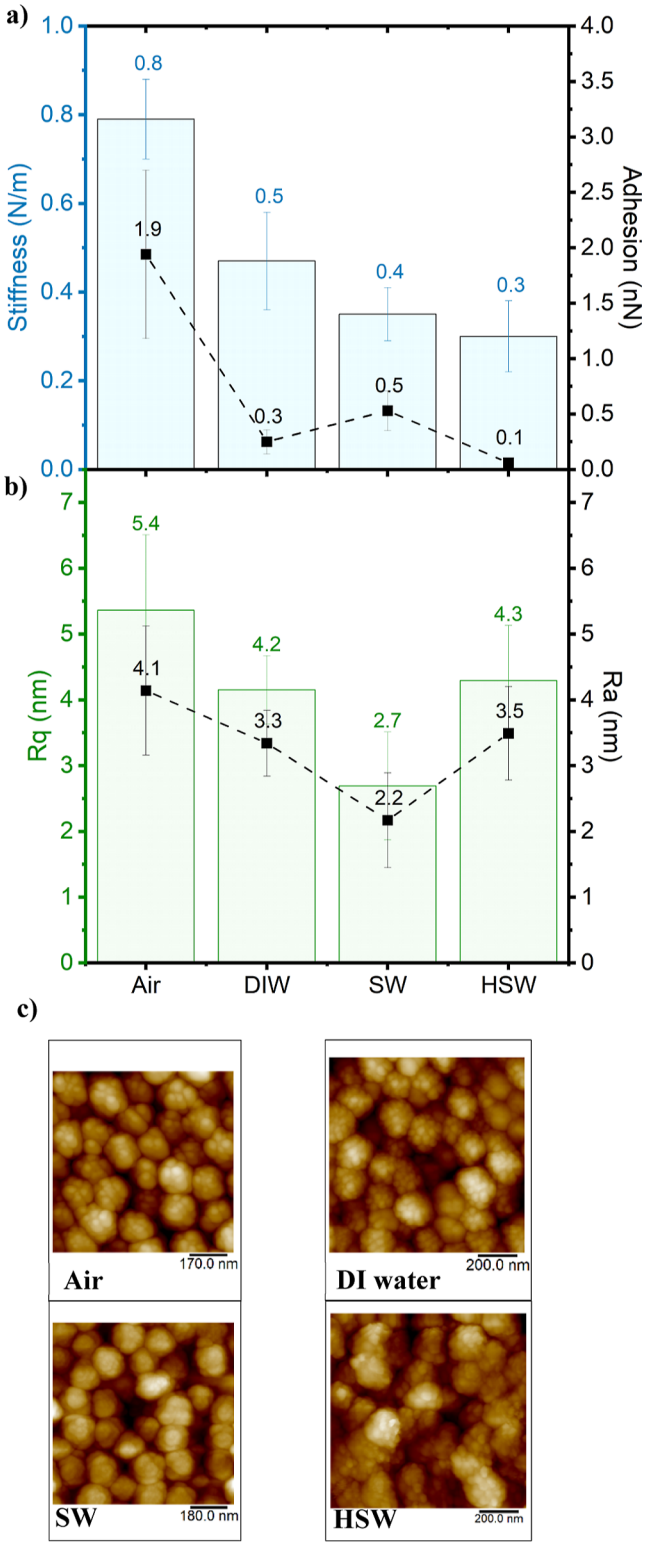

Figure 6. (a) QNM properties (stiffness and adhesion) for the brush-grafted NPs, S31+; (b) roughness (R_q and R_a) in air, DI water, SW ($I \sim 1.14$ M), and HSW ($I \sim 2.5$ M) using a AFM-peak force tapping mode; and (c) corresponding images.

water, respectively). Raspberry-like globules are observed for the brush-bearing NPs in both dry and DI water, which is consistent with the SEM images and consistent with a collapsed, "mushroom-like" brush structure. When the nanomechanical properties of the NPs are compared before and after grafting of the polyelectrolyte chains, the brush-bearing NPs in the collapsed state show a decreased adhesive force (from 3 nN for the PS core to 1.9 nN) for the brush-grafted NPs in dry conditions; the corresponding values for the same systems in DI water are 0.5 and 0.3 nN, respectively. In addition, the stiffness of the brush-grafted NPs in the collapsed state is similar to that of the core (~0.8 and 0.5 N/m in dry and DI water, respectively). The presence of CBs increases the surface roughness to 5.4 nm. Upon entering the end of the swollen state in SW ($I \sim 1.14$ M) and exposure of the underlying PS surface reduces adhesion to ~0.5 nN, which is comparable to what was observed previously for the PS core. Swelling and extension of the chains in lateral and normal directions reduce the number of globules on the surface, which lowers the surface roughness from 4.2 to 2.7 nm for the brushes in the wet CB and OB regimes, respectively. The brushes collapse back upon exposure to higher salt concentrations (e.g., in the SB regime at high salt concentration, the surface roughness increases slightly to 4.3 nm with a reduction in the adhesion and stiffness to 0.1 nN and 0.3 N/m, respectively). This is due to the adsorption of salt ions to the exterior of the brush and is consistent with previous reports of decreased adhesion with increasing salt concentration.[64] Table 2 summarizes the roughness and

Table 2. Summary of Roughness (Root Mean Square, R_q), Stiffness, and Adhesion for the PS Core and Brush-Bearing NPs in Various Regimes[a]

system	size (nm)	roughness (R_q) (nm)	stiffness (N/m)	adhesion (nN)
PS core	91 ± 8	1.8 ± 0.4	0.6 ± 0.2	0.5 ± 0.2
S31+ (CB)	125 ± 6	4.2 ± 0.5	0.5 ± 0.1	0.3 ± 0.1
S31+ (OB)	147 ± 1.2	2.7 ± 0.8	0.4 ± 0.1	0.5 ± 0.2
S31+ (SB)	156 ± 15	4.3 ± 0.8	0.3 ± 0.1	0.1 ± 0.03

[a]All measurements are done in liquid environments (CB in DI water, OB in SW, and SB in HSW).

nanomechanical properties for the pristine PS core and the decorated NPs at the various regimes. The salt-induced swelling and the corresponding nanomechanical response in the presence of different salts (NaCl, Na_2SO_4, and $MgCl_2$) are shown in Figure 7, which is summarized from the distributions in Figure S10. The ability to resist elastic compression and deformation of the surface-grafted polyelectrolyte patches depends on the charge density, typical to what is observed in other pH and salt-responsive polymers.[65,66] As shown in Figure 7g, in the CB state, where the counterion concentration is low, the patches are soft with a reported stiffness value of ~0.5 N/m in DI water. Upon entering the OB regime in NaCl at 0.1 M, chain swelling and ion diffusion increase the charge density within the network and increase the stiffness to 0.6 N/m similar to porous ladder-like structures.[67] At the transition region between OB and SB at 1 M, a reduction in the charge density within the network by ion expulsion reduces the stiffness to 0.2 N/m. As the IS increases to 2.5 M, the charge density within the brush network drops, but the external salt association retains its stiffness to 0.4 N/m. When the particles are immersed in solutions with IS ~ 0.1−0.5 M, brush swelling results in a smoother surface with gradual reduction in roughness. The raspberry-like globules start reappearing at 2.5 M as the brush retracts coupled with a surface roughness

https://doi.org/10.1021/acs.langmuir.3c03713
Langmuir 2024, 40, 5837−5849

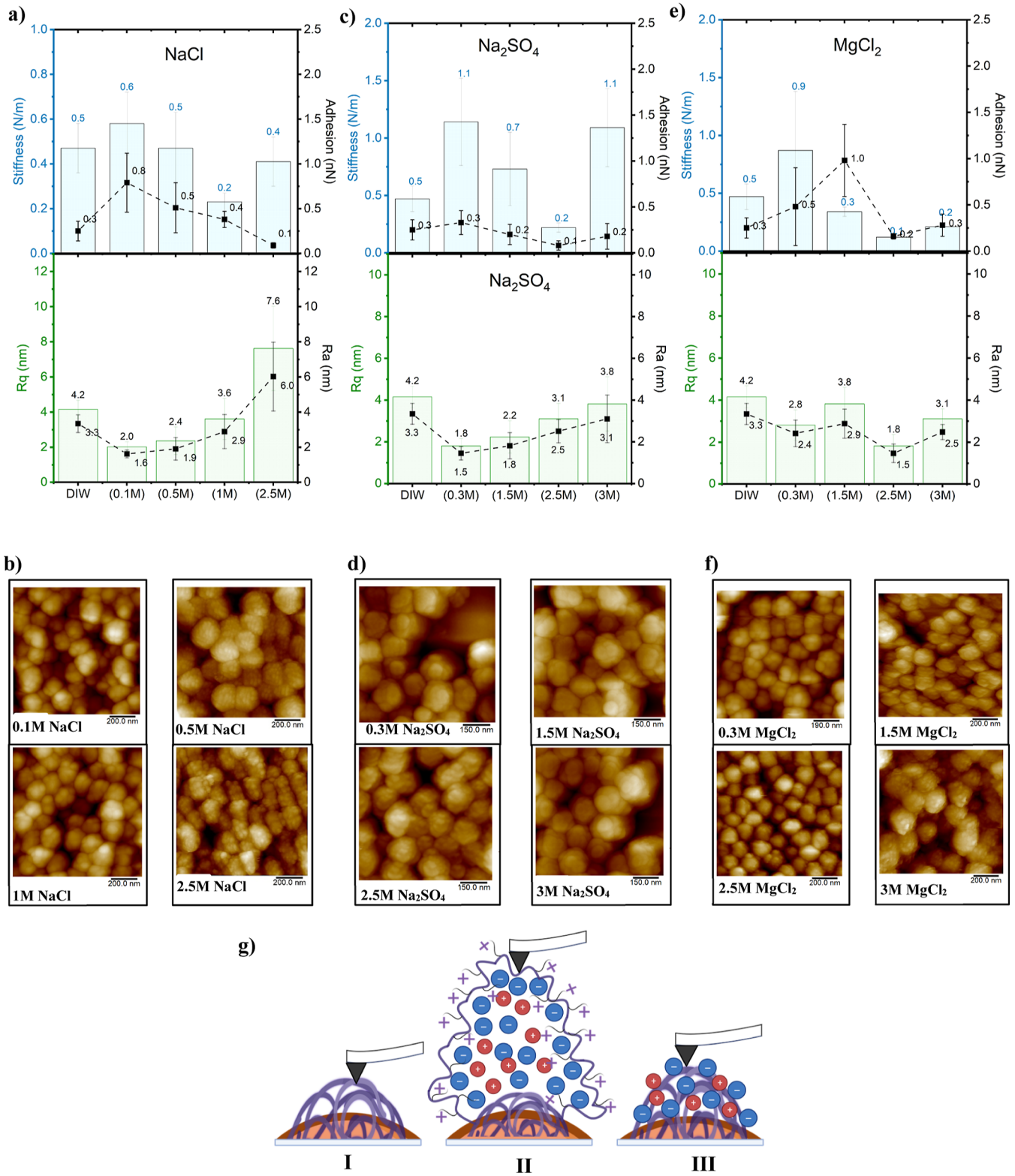

Figure 7. QNM properties, roughness values for S31+, and the corresponding AFM images in (a,b) NaCl (0.1, 0.5, 1, and 2.5 M), (c,d) Na_2SO_4 (0.3, 1.5, 2.5, 3 M), and (e,f) $MgCl_2$ (0.3, 1.5, 2.5, 3 M); and (g) schematic of the AFM tip and the various conformational regimes (I) CB, (II) OB, and (III) SB.

increase, which is more pronounced in NaCl compared to the increase in roughness in other salts at an equivalent IS (i.e., SW and 2.5 M Na_2SO_4). Similar trends are seen for sodium sulfate in Figure 7c,d, with gradual reduction in surface roughness in the OB regime and retention of the globules in the SB regime. However, the larger size of SO_4^{2-} ions prevents the collapsed coils from becoming fully restored. It is worth noting that the low surface roughness is accompanied by a stronger adhesive force and vice versa; hence, modulating swelling thresholds allows for control of the NP surface properties.

https://doi.org/10.1021/acs.langmuir.3c03713
Langmuir 2024, 40, 5837−5849

CONCLUSIONS

Surface grafting of PGMA-based polyelectrolyte brushes on PS cores dramatically increases the colloidal stability of the particles especially at high-temperature and high-salinity conditions. A seeded emulsion polymerization method is used to synthesize the PS cores followed by swelling and polymerization with GMA using DVB as a cross-linker. A two-step amination process of the PGMA epoxide groups first with EDA and then with trimethyl glycidyl ammonium chloride leads to grafting of positively charged polyelectrolyte brushes on the NP cores. The grafting density of the brushes is controlled by varying the molar ratio of PS:PGMA (e.g., 2:1, 3:1, and 4:1 corresponding to S21+, S31+, and S41+, respectively).

The size and colloidal stability of the different NP systems were studied and correlated with salt adsorption measurements by QCM-D and nanomechanical properties obtained by AFM under both dry and wet conditions using a liquid cell. The size and colloidal stability are consistent with the different structure configurations proposed for polyelectrolyte brushes. In dry conditions or when no salt is present (DI water), the brushes adopt a collapsed, "mushroom-like" configuration (CB). The addition of ions up to ∼1 M swells the brushes, which enter the OB regime. The swelling and salt uptake capacity depend on the IS and the hydration ability of the ions. At high IS (1−2.5 M), local charge saturation/condensation occurs, and ion expulsion contracts, the brushes back into a collapsed conformation (SB state), and the surface globules reappear. QCM-D measurements are consistent with the above. A gradual increase in salt adsorption is seen with the increasing IS as the brushes move from the CB configuration to the OB configuration, followed by a reduction in salt adsorption as the brushes transition from the OB to SB states. When they reach the SB state, the brushes collapse, but they continue to adsorb ions predominantly on the exterior of the brushes. Salt absorption on the surface increases the surface roughness and decreases the adhesion of the samples with the AFM tip due to the increased rigidity of the brush supported by the surrounding salt ions. The information obtained from this study further advances our understanding of the behavior of salt-responsive brushes tethered on NP surfaces and will enable advancements in various fields requiring stable colloidal suspensions, especially in high-salt/high-temperature environments with adaptive swelling thresholds that can ultimately control and modulate surface properties.

ASSOCIATED CONTENT

Supporting Information

The Supporting Information is available free of charge at https://pubs.acs.org/doi/10.1021/acs.langmuir.3c03713.

Salt composition of seawater and high-salinity water; FTIR spectra for the PS core and S31+ [PS-PGMA-EDA-Q+ (3:1)]; TGA (wt %) change and derivative weight change (wt %/°C); size distribution measurements obtained from DLS of the PS core and the brush-grafted NPs with different grafting densities; transmission profiles across the sample as a function of time at 1000 rpm; transmission profile in seawater at 25 °C; separation indices calculated from the respective transmission profiles; AFM images of S31+ NPs covered with a droplet of various salt solutions and the corresponding size measurements; change in frequency (ΔF) and dissipation (ΔD) as a function of time for S31+ drop-casted on Au-coated quartz sensors with a continuous flow; experimentally measured and modeled frequency profiles from QCM-D with the estimated areal mass (salt adsorption); and stiffness and adhesion distributions calculated from the force−separation plots (PDF)

AUTHOR INFORMATION

Corresponding Author

Emmanuel P. Giannelis − *Materials Science and Engineering, Cornell University, Ithaca, New York 14853, United States*; Email: epg2@cornell.edu

Authors

Bashayer Saad Aldakkan − *Materials Science and Engineering, Cornell University, Ithaca, New York 14853, United States*; orcid.org/0000-0001-9025-540X

Nikolaos Chalmpes − *Materials Science and Engineering, Cornell University, Ithaca, New York 14853, United States*; orcid.org/0000-0003-2744-5934

Genggeng Qi − *Materials Science and Engineering, Cornell University, Ithaca, New York 14853, United States*

Mohamed Amen Hammami − *Materials Science and Engineering, Cornell University, Ithaca, New York 14853, United States*; orcid.org/0000-0002-6162-3629

Mazen Yousef Kanj − *College of Petroleum Engineering & Geosciences, King Fahd University of Petroleum & Minerals, Dhahran 31261, Saudi Arabia*; orcid.org/0000-0002-2674-4505

Complete contact information is available at: https://pubs.acs.org/10.1021/acs.langmuir.3c03713

Author Contributions

B.S.A. proposed and conducted the experiments and modeling and wrote the manuscript draft. N.C. assisted the AFM data and experiment methodology. G.Q. and M.A.H. advised on nanoparticle synthesis. M.Y.Z. advised on the conditions for field application. E.P.G. guided the work, reviewed, and revised the manuscript. All authors discussed and commented on the manuscript.

Funding

This publication is based on work supported by the College of Petroleum Engineering and Geosciences, King Fahd University of Petroleum and Minerals.

Notes

The authors declare no competing financial interest.

ACKNOWLEDGMENTS

B.S.A. would like to acknowledge Saudi Aramco and EXPEC-Advanced Research Center (ARC) for the graduate scholarship. The authors would like to thank Antonios Kouloumpis for guidance on AFM measurements and Ahmed Alsmaeil for his assistance in the TEM image and optimization of LUMiSizer data. This work made use of the Cornell Center for Materials Research Shared Facilities which are supported through the NSF MRSEC program (DMR-1719875). Schematics were generated with BioRender. Chemical reactions were produced with ChemDraw.

ABBREVIATIONS

PS, polystyrene; NPs, nanoparticles; DIW, deionized water; GMA, glycidyl methacrylate; EDA, ethylene diamine;

GTMAC, glycidyltrimethylammonium chloride; AOETMAC, 2-(acryloyloxy)ethyl]trimethylammonium chloride solution; V50, 2,2′-azobis(2-methylpropionamidine) dihydrochloride; THF, tetrahydrofuran; DVB, divinylbenzene; DLS, dynamic light scattering; SEM, scanning electron microscopy; TEM, transmission electron microscopy; AFM, atomic force microscopy; LUMiSizer, dispersion analyzer; TGA, thermogravimetric analysis; FTIR, Fourier-transform infrared spectroscopy; QCM-D, quartz crystal microbalance with dissipation monitoring sample S41, functionalized PS:PGMA NPs with mole ratio (4:1); sample S31, functionalized PS:PGMA NPs with a mole ratio of 3:1; sample S21, functionalized PS:PGMA NPs with a mole ratio of 2:1; CB, collapsed brush; OB, osmotic brush; SB, salted brush; F−S, force−separation curves; SW, seawater; HSW, high-salinity water.

REFERENCES

(1) Rad, M. E.; Soylukan, C.; Kulabhusan, P. K.; Günaydın, B. N.; Yüce, M. Material and Design Toolkit for Drug Delivery: State of the Art, Trends, and Challenges. *ACS Appl. Mater. Interfaces* **2023**, *15* (48), 55201−55231.

(2) Liu, Y.; Liu, J.; Chen, D.; Wang, X.; Liu, Z.; Liu, H.; Jiang, L.; Wu, C.; Zou, Y. Quinoxaline-Based Semiconducting Polymer Dots for in Vivo NIR-II Fluorescence Imaging. *Macromolecules* **2019**, *52* (15), 5735−5740.

(3) Griffiths, M. Z.; Shinoda, W. Analyzing the Role of Surfactants in the Colloidal Stability of Nanoparticles in Oil through Coarse-Grained Molecular Dynamics Simulations. *J. Phys. Chem. B* **2021**, *125*, 6315−6321.

(4) Hannington, M.; Harðardóttir, V.; Garbe-Schönberg, D.; Brown, K. L. Gold Enrichment in Active Geothermal Systems by Accumulating Colloidal Suspensions. *Nat. Geosci.* **2016**, *9* (4), 299−302.

(5) Hueckel, T.; Luo, X.; Aly, O. F.; Macfarlane, R. J. Nanoparticle Brushes: Macromolecular Ligands for Materials Synthesis. *Acc. Chem. Res.* **2023**, *56* (14), 1931−1941.

(6) Snee, P. T. The Role of Colloidal Stability and Charge in Functionalization of Aqueous Quantum Dots. *Acc. Chem. Res.* **2018**, *51* (11), 2949−2956.

(7) Smith, G. N.; Finlayson, S. D.; Rogers, S. E.; Bartlett, P.; Eastoe, J. Electrolyte-Induced Instability of Colloidal Dispersions in Nonpolar Solvents. *J. Phys. Chem. Lett.* **2017**, *8*, 4668−4672.

(8) Napper, D. H. *Polymeric Stabilization of Colloidal Dispersions*; Academic Pr, 1983.

(9) Russel, W. B.; Saville, D. A.; Schowalter, W. R. *Colloidal Dispersions*; Cambridge University Press: Cambridge, 1989.

(10) Worthen, A. J.; Tran, V.; Cornell, K. A.; Truskett, T. M.; Johnston, K. P. Steric Stabilization of Nanoparticles with Grafted Low Molecular Weight Ligands in Highly Concentrated Brines Including Divalent Ions. *Soft Matter* **2016**, *12* (7), 2025−2039.

(11) Halperin, A.; Kröger, M.; Zhulina, E. B. Colloid-Brush Interactions: The Effect of Solvent Quality. *Macromolecules* **2011**, *44*, 3622−3638.

(12) Zhang, L.; Bei, H. P.; Piao, Y.; Wang, Y.; Yang, M.; Zhao, X. Polymer-Brush-Grafted Mesoporous Silica Nanoparticles for Triggered Drug Delivery. *ChemPhysChem* **2018**, *19* (16), 1956−1964.

(13) Ding, Z.; Chen, C.; Yu, Y.; de Beer, S. Synthetic Strategies to Enhance the Long-Term Stability of Polymer Brush Coatings. *J. Mater. Chem. B* **2022**, *10*, 2430−2443.

(14) Liu, T.; Yan, S.; Zhou, R.; Zhang, X.; Yang, H.; Yan, Q.; Yang, R.; Luan, S. Self-Adaptive Antibacterial Coating for Universal Polymeric Substrates Based on a Micrometer-Scale Hierarchical Polymer Brush System. *ACS Appl. Mater. Interfaces* **2020**, *12*, 42576−42585.

(15) Zhao, Y.; Wu, H.; Yin, R.; Yu, C.; Matyjaszewski, K.; Bockstaller, M. R. Copolymer Brush Particle Hybrid Materials with "Recall-and-Repair" Capability. *Chem. Mater.* **2023**, *35* (17), 6990−6997.

(16) Yang, L.; Xu, J.; Wang, J.; Lang, F.; Liu, B.; Yang, Z. Responsive Single-Chain/Colloid Composite Janus Nanoparticle. *Macromolecules* **2020**, *53* (6), 2264−2270.

(17) Wang, C.; Zhao, H. Polymer Brushes and Surface Nanostructures: Molecular Design, Precise Synthesis, and Self-Assembly. *Langmuir* **2024**, *40* (5), 2439−2464.

(18) Kim, S.; Kwak, H.; Choi, I.; Hwang, J.; Kwon, B.; Lee, E.; Ye, J.; Lim, H.; Cho, K.; Chung, H.-J.; Lee, W. H. Enhanced Gas Sensing Properties of Graphene Transistor by Reduced Doping with Hydrophobic Polymer Brush as a Surface Modification Layer. *ACS Appl. Mater. Interfaces* **2020**, *12*, 55493−55500.

(19) Li, T.-H.; Yadav, V.; Conrad, J. C.; Robertson, M. L. Effect of Dispersity on the Conformation of Spherical Polymer Brushes. *ACS Macro Lett.* **2021**, *10*, 518−524.

(20) Metze, F. K.; Sant, S.; Meng, Z.; Klok, H.-A.; Kaur, K. Swelling-Activated, Soft Mechanochemistry in Polymer Materials. *Langmuir* **2023**, *39* (10), 3546−3557.

(21) Aldakkan, B. S.; Hammami, M. A.; Qi, G.; Kanj, M. Y.; Giannelis, E. P. Stimuli-Responsive, Hydrolyzable Poly(Vinyl Laurate-Co-Vinyl Acetate) Nanoparticle Platform for In Situ Release of Surfactants. *ACS Appl. Mater. Interfaces* **2021**, *13* (21), 25553−25562.

(22) Ehtiati, K.; Moghaddam, S. Z.; Klok, H.-A.; Daugaard, A. E.; Thormann, E. Specific Counterion Effects on the Swelling Behavior of Strong Polyelectrolyte Brushes. *Macromolecules* **2022**, *55* (12), 5123−5130.

(23) Eygeris, Y.; Ulery, N.; Zharov, I. PH-Responsive Membranes from Self-Assembly of Poly(2-(Dimethylamino)Ethyl Methacrylate) Brush Silica Nanoparticles. *Langmuir* **2023**, *39* (44), 15792−15798.

(24) Zhang, L.; Bei, H. P.; Piao, Y.; Wang, Y.; Yang, M.; Zhao, X. Polymer-Brush-Grafted Mesoporous Silica Nanoparticles for Triggered Drug Delivery. *ChemPhysChem* **2018**, *19* (16), 1956−1964.

(25) Nastyshyn, S.; Stetsyshyn, Y.; Raczkowska, J.; Nastishin, Y.; Melnyk, Y.; Panchenko, Y.; Budkowski, A. Temperature-Responsive Polymer Brush Coatings for Advanced Biomedical Applications. *Polymers* **2022**, *14* (19), 4245.

(26) Besford, Q. A.; Merlitz, H.; Schubotz, S.; Yong, H.; Chae, S.; Schnepf, M. J.; Weiss, A. C. G.; Auernhammer, K.; Sommer, J.-U.; Uhlmann, P.; Fery, A. Mechanofluorescent Polymer Brush Surfaces That Spatially Resolve Surface Solvation. *ACS Nano* **2022**, *16*, 3383−3393.

(27) Li, S.; Zhang, Z.; Hou, G.; Liu, J.; Gao, Y.; Coates, P.; Zhang, L. Self-Assembly and Structural Manipulation of Diblock-Copolymer Grafted Nanoparticles in a Homopolymer Matrix †. *Phys. Chem. Chem. Phys.* **2019**, *21*, 11785−11796.

(28) Choi, J.; Hui, C. M.; Pietrasik, J.; Dong, H.; Matyjaszewski, K.; Bockstaller, M. R. Toughening Fragile Matter: Mechanical Properties of Particle Solids Assembled from Polymer-Grafted Hybrid Particles Synthesized by ATRP. *Soft Matter* **2012**, *8* (15), 4072−4082.

(29) Lotierzo, A.; Longbottom, B. W.; Lee, W. H.; Bon, S. A. F. Synthesis of Janus and Patchy Particles Using Nanogels as Stabilizers in Emulsion Polymerization. *ACS Nano* **2019**, *13* (1), 399−407.

(30) Foster, J. C.; Yoon, A.; Lyons, K.; Martinez, E. J.; Leguizamon, S. C.; Bezik, C. T.; Frischknecht, A. L.; Redline, E. M. Unexpected Thermomechanical Behavior of Off-Stoichiometry Epoxy/Amine Materials. *Macromolecules* **2023**, *56* (8), 3183−3194.

(31) Bhagat, M. N.; Bennett, C. K.; Chang, G.-F.; Zhu, Y.; Raghuraman, A.; Belowich, M. E.; Nguyen, S. T.; Broadbelt, L. J.; Notestein, J. M. Enhancing the Regioselectivity of B(C6F5)3-Catalyzed Epoxide Alcoholysis Reactions Using Hydrogen-Bond Acceptors. *ACS Catal.* **2019**, *9* (10), 9663−9670.

(32) Eisavi, R.; Karimi, A. $CoFe_2O_4/Cu(OH)_2$ magnetic nanocomposite: an efficient and reusable heterogeneous catalyst for one-pot synthesis of β-hydroxy-1,4-disubstituted-1,2,3-triazoles from epoxides. *RSC Adv.* **2019**, *9* (51), 29873−29887.

(33) Liu, X.; Jiang, C.; Ren, C.; Li, Z. Controlled Ring-Opening Polymerization of Epoxides Catalyzed by Metal-Free Phosphazenium

https://doi.org/10.1021/acs.langmuir.3c03713
Langmuir 2024, 40, 5837−5849

Salts (P5+): Using Carboxylic Acid as an Initiator to Prepare Esterified Polyethers. *ACS Appl. Polym. Mater.* **2024**, *6* (1), 896−904.
(34) Jin, K.; Heath, W. H.; Torkelson, J. M. Kinetics of Multifunctional Thiol-Epoxy Click Reactions Studied by Differential Scanning Calorimetry: Effects of Catalysis and Functionality. *Polymer* **2015**, *81*, 70−78.
(35) Bonollo, S.; Lanari, D.; Vaccaro, L. Ring-Opening of Epoxides in Water. *Eur. J. Org Chem.* **2011**, *2011* (14), 2587−2598.
(36) Puretskiy, N.; Ionov, L. Synthesis of Robust Raspberry-like Particles Using Polymer Brushes. *Langmuir* **2011**, *27*, 3006−3011.
(37) Cheraghian, G.; Rostami, S.; Afrand, M. Nanotechnology in Enhanced Oil Recovery. *Processes* **2020**, *8*, 1073.
(38) Gong, Z.; Li, N.; Qin, M.; Kang, W.; Yang, S. Magnetic Nano-Fe3O4-Based Oleophilic Tracer for Stability Studies of Nano-Tracer in Oilfields Condition. *Colloids Surf., A* **2024**, *683*, 133085.
(39) Ugelstad, J.; Mórk, P.; Kaggerud, K. H.; Ellingsen, T.; Berge, A. Swelling of Oligomer-Polymer Particles. New Methods of Preparation. *Adv. Colloid Interface Sci.* **1980**, *13* (1−2), 101−140.
(40) Shen, Y.; Du, C.; Zhou, J.; Ma, F. The Facile Modification of Polyacrylate Emulsion via Hexadecane to Enhance Controlled-Release Profiles of Coated Urea. *Sci. Rep.* **2018**, *8* (1), 12279.
(41) Voinova, M. V.; Rodahl, M.; Jonson, M.; Kasemo, B. Viscoelastic Acoustic Response of Layered Polymer Films at Fluid-Solid Interfaces: Continuum Mechanics Approach. *Phys. Scr.* **1999**, *59* (5), 391−396.
(42) Cho, N.-J.; Kanazawa, K. K.; Glenn, J. S.; Frank, C. W. Employing Two Different Quartz Crystal Microbalance Models To Study Changes in Viscoelastic Behavior upon Transformation of Lipid Vesicles to a Bilayer on a Gold Surface. *Anal. Chem.* **2007**, *79* (18), 7027−7035.
(43) Pereira, D.; Santamaria, A.; Pawar, N.; Carrascosa-Tejedor, J.; Sardo, M.; Mafra, L.; Guzmán, E.; Owen, D. J.; Zaccai, N. R.; Maestro, A.; Marín-Montesinos, I. Engineering Phosphatidylinositol-4,5-Bisphosphate Model Membranes Enriched in Endocytic Cargo: A Neutron Reflectometry, AFM and QCM-D Structural Study. *Colloids Surf., B* **2023**, *227*, 113341.
(44) Hammami, M. A.; Kouloumpis, A.; Qi, G.; Alsmaeil, A. W.; Aldakkan, B.; Kanj, M. Y.; Giannelis, E. P. Probing the Mechanism of Targeted Delivery of Molecular Surfactants Loaded into Nanoparticles after Their Assembly at Oil-Water Interfaces. *ACS Appl. Mater. Interfaces* **2023**, *15* (4), 6113−6122.
(45) Heyda, J.; Muzdalo, A.; Dzubiella, J. Rationalizing Polymer Swelling and Collapse under Attractive Cosolvent Conditions. *Macromolecules* **2013**, *46* (3), 1231−1238.
(46) Sing, C. E.; Zwanikken, J. W.; Olvera De La Cruz, M. Effect of Ion-Ion Correlations on Polyelectrolyte Gel Collapse and Reentrant Swelling. *Macromolecules* **2013**, *46* (12), 5053−5065.
(47) Metze, F. K.; Sant, S.; Meng, Z.; Klok, H.-A.; Kaur, K. Swelling-Activated, Soft Mechanochemistry in Polymer Materials. *Langmuir* **2023**, *39* (10), 3546−3557.
(48) Landsgesell, J.; Beyer, D.; Hebbeker, P.; Košovan, P.; Holm, C. The PH-Dependent Swelling of Weak Polyelectrolyte Hydrogels Modeled at Different Levels of Resolution. *Macromolecules* **2022**, *55* (8), 3176−3188.
(49) Hollingsworth, N. R.; Wilkanowicz, S. I.; Larson, R. G. Salt- and PH-Induced Swelling of a Poly(Acrylic Acid) Brush via Quartz Crystal Microbalance w/Dissipation (QCM-D). *Soft Matter* **2019**, *15* (39), 7838−7851.
(50) Chu, X.; Yang, J.; Liu, G.; Zhao, J. Swelling Enhancement of Polyelectrolyte Brushes Induced by External Ions. *Soft Matter* **2014**, *10* (30), 5568−5578.
(51) Zhulina, E.; Singh, C.; Balazs, A. C. Behavior of Tethered Polyelectrolytes in Poor Solvents. *J. Chem. Phys.* **1998**, *108* (3), 1175−1183.
(52) Yang, Y.; Zhao, H. Water-Induced Polymer Swelling and Its Application in Soft Electronics. *Appl. Surf. Sci.* **2022**, *577*, 151895.
(53) Rahmaninejad, H.; Parnell, A. J.; Chen, W.-L.; Duzen, N.; Sexton, T.; Dunderdale, G.; Ankner, J. F.; Bras, W.; Ober, C. K.; Ryan, A. J.; Ashkar, R. Synthesis and Characterization of Stimuli-Responsive Polymer Brushes in Nanofluidic Channels. *ACS Appl. Mater. Interfaces* **2023**, *15* (47), 54942−54951.
(54) Zhong, C.; Yida, D.; Hu, W.; Qiao, J.; Zhang, L.; Zhang, J. A Review of Electrolyte Materials and Compositions for Electrochemical Supercapacitors. *Chem. Soc. Rev.* **2015**, *44*, 7484.
(55) Nose, A.; Hojo, M.; Ueda, T. Effects of Salts, Acids, and Phenols on the Hydrogen-Bonding Structure of Water-Ethanol Mixtures. *J. Phys. Chem. B* **2004**, *108* (2), 798−804.
(56) Horst, R. J.; Brió Pérez, M.; Cohen, R.; Cirelli, M.; Dueñas Robles, P. S.; Elshof, M. G.; Andreski, A.; Hempenius, M. A.; Benes, N. E.; Damen, C.; de Beer, S. Swelling of Poly(Methyl Acrylate) Brushes in Acetone Vapor. *Langmuir* **2020**, *36* (40), 12053−12060.
(57) Prusty, D.; Gallegos, A.; Wu, J. Unveiling the Role of Electrostatic Forces on Attraction between Opposing Polyelectrolyte Brushes. *Langmuir* **2024**, *40* (4), 2064−2078.
(58) Brettmann, B.; Pincus, P.; Tirrell, M. Lateral Structure Formation in Polyelectrolyte Brushes Induced by Multivalent Ions. *Macromolecules* **2017**, *50* (3), 1225−1235.
(59) Ishida, N.; Biggs, S. Salt-Induced Structural Behavior for Poly(N-Isopropylacryamide) Grafted onto Solid Surface Observed Directly by AFM and QCM-D. *Macromolecules* **2007**, *40* (25), 9045−9052.
(60) Patra, C. N.; Yethiraj, A. Density Functional Theory for the Nonspecific Binding of Salt to Polyelectrolytes: Thermodynamic Properties. *Biophys. J.* **2000**, *78* (2), 699−706.
(61) Nguyen, T. T.; Grosberg, A. Yu.; Shklovskii, B. I. Screening of a Charged Particle by Multivalent Counterions in Salty Water: Strong Charge Inversion. *J. Chem. Phys.* **2000**, *113* (3), 1110−1125.
(62) Sun, Y.; Akhremitchev, B.; Walker, G. C. Using the Adhesive Interaction between Atomic Force Microscopy Tips and Polymer Surfaces to Measure the Elastic Modulus of Compliant Samples. *Langmuir* **2004**, *20* (14), 5837−5845.
(63) Payam, A. F. Modeling and Analysis of the Capillary Force for Interactions of Different Tip/Substrate in AFM Based on the Energy Method. *ACS Meas. Sci. Au* **2023**, *3*, 194−199.
(64) Alfhaid, L.; Williams, N. H.; Geoghegan, M. Adhesion between Oppositely Charged Polyelectrolytes in Salt Solution. *J. Appl. Polym. Sci.* **2020**, *137* (38), 49130.
(65) Nyström, L.; Álvarez-Asencio, R.; Frenning, G.; Saunders, B. R.; Rutland, M. W.; Malmsten, M. Electrostatic Swelling Transitions in Surface-Bound Microgels. *ACS Appl. Mater. Interfaces* **2016**, *8* (40), 27129−27139.
(66) Nyström, L.; Nordström, R.; Bramhill, J.; Saunders, B. R.; Álvarez-Asencio, R.; Rutland, M. W.; Malmsten, M. Factors Affecting Peptide Interactions with Surface-Bound Microgels. *Biomacromolecules* **2016**, *17* (2), 669−678.
(67) Słowikowska, M.; Wolski, K.; Wójcik, A. J.; Wesner, D.; Schönherr, H.; Zapotoczny, S. Unraveling the Nanomechanical Properties of Surface-Grafted Conjugated Polymer Brushes with Ladder-like Architecture. *Polym. Chem.* **2020**, *11* (44), 7050−7062.

https://doi.org/10.1021/acs.langmuir.3c03713
Langmuir 2024, 40, 5837−5849